1 **Photosensitized Electrospun Nanofibrous Filters for Capturing and Killing Airborne**

2 **Coronaviruses under Visible Light Irradiation**

3

4 Hongchen Shen,[1#] Zhe Zhou,[1#] Haihuan Wang,[1#] Mengyang Zhang,[1] Minghao Han,[2] Yun Shen,[2*]

5 Danmeng Shuai[1*]

6

7 1 Department of Civil and Environmental Engineering, The George Washington University,

8 Washington, D. C., 20052

9 2 Department of Chemical and Environmental Engineering, University of California, Riverside,

10 Riverside, C. A., 92521

11

12 # Equal Contribution.

13 * Corresponding Authors:

14 Danmeng Shuai: Phone: 202-994-0506, Fax: 202-994-0127, Email: danmengshuai@gwu.edu,

15 Website: http://materwatersus.weebly.com/

16 Yun Shen: Phone: 951-827-2423, Fax: 951-827-5696, Email: yun.shen@ucr.edu, Website:

17 https://yunshen.weebly.com/

18

19

20

Abstract

To address the challenge of the airborne transmission of SARS-CoV-2, photosensitized electrospun nanofibrous membranes were fabricated to effectively capture and inactivate coronavirus aerosols. With an ultrafine fiber diameter (~ 200 nm) and a small pore size (~ 1.5 µm), the optimized membranes caught 99.2% of the aerosols of the murine hepatitis virus A59 (MHV-A59), a coronavirus surrogate for SARS-CoV-2. In addition, rose bengal was used as the photosensitizer for the membranes because of its excellent reactivity in generating virucidal singlet oxygen, and the membranes rapidly inactivated 98.9% of MHV-A59 in virus-laden droplets only after 15 min irradiation of simulated reading light. Singlet oxygen damaged the virus genome and impaired virus binding to host cells, which elucidated the mechanism of disinfection at a molecular level. Membrane robustness was also evaluated, and no efficiency reduction for filtering MHV-A59 aerosols was observed after the membranes being exposed to both indoor light and sunlight for days. Nevertheless, sunlight exposure photobleached the membranes, reduced singlet oxygen production, and compromised the performance of disinfecting MHV-A59 in droplets. In contrast, the membranes after simulated indoor light exposure maintained their excellent disinfection performance. In summary, photosensitized electrospun nanofibrous membranes have been developed to capture and kill airborne environmental pathogens under ambient conditions, and they hold promise for broad applications as personal protective equipment and indoor air filters.

43   **Synopsis**

44   Photosensitized electrospun nanofibrous filters with excellent capture-and-kill performance

45   against coronaviruses were designed and implemented to prevent the airborne transmission of

46   COVID-19.

47

48   **Table of Contents**

49

50

51

52

53

54
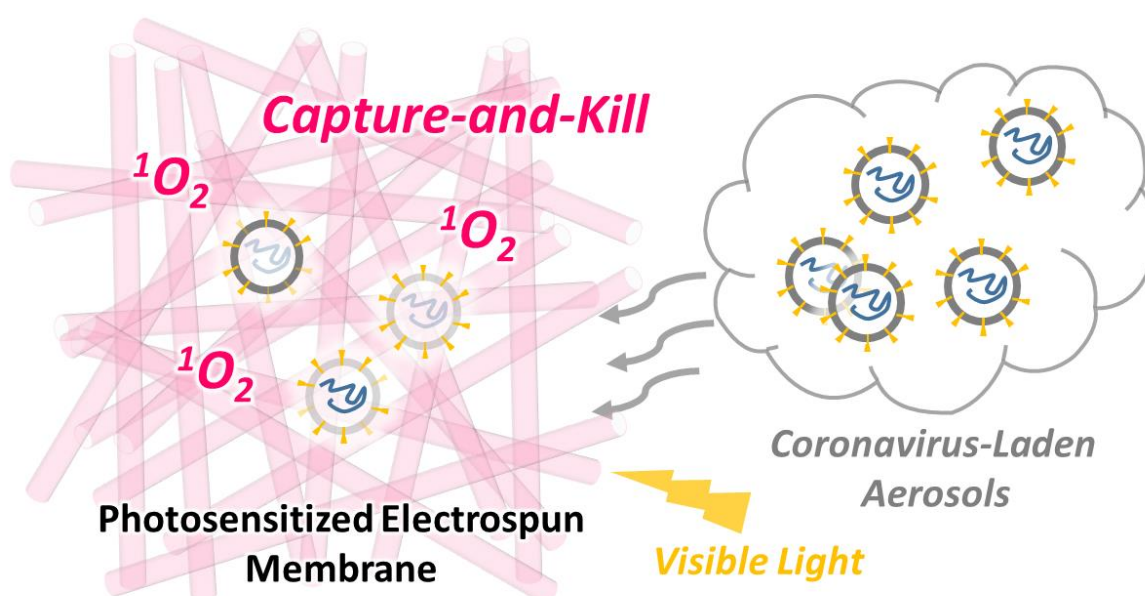
1. Introduction

56 Airborne transmission of SARS-CoV-2 has been recognized as an important route for spreading

57 COVID-19 by the World Health Organization and the U.S. Centers for Disease Control and

58 Prevention.[1,2] SARS-CoV-2 aerosols could suspend, accumulate, and remain infectious in the air

59 for a long duration up to hours.[3] To reduce the transmission of SARS-CoV-2 through aerosols,

60 physical barriers like face masks and indoor air filters have been successfully implemented. In

61 particular, numerous studies have emphasized the important role of wearing masks in reducing the

62 spread of COVID-19.[4–6] Electrospinning has emerged as a promising nanotechnology for

63 developing non-woven, ultrafine fibrous membranes that are excellent for removing aerosols.[7–9]

64 The electrospun membranes have a reduced pore size (tens of nanometers to several micrometers),

65 an increased specific surface area, and enhanced porosity to enable efficient aerosol filtration and

66 a low pressure drop in filtration.[7] Furthermore, the surface and volume charges within the

67 electrospun membranes improve aerosol filtration through electrostatic attraction.[10,11] Particularly,

68 our previous study has underscored that the electrospun membranes caught up to 99.9% of

69 coronavirus aerosols whose size was within or close to that of the most penetrating particles in

70 mechanical air filtration.[12] However, like most masks and air filters currently used on the market,

71 electrospun membranes only physically capture viral aerosols but they do not inactivate the viruses,

72 which could lead to secondary contamination and potential infection (e.g., via the contact of the

73 contaminated masks/air filters or viruses dislodged from the masks/filters).[13]

74

75 The goal of our study is to (i) develop highly efficient and robust photosensitized electrospun

76 nanofibrous membranes that can both physically capture and chemically disinfect coronavirus

77 aerosols, and (ii) elucidate the mechanism of photooxidation and inactivation of coronaviruses at

4

78   a molecular level. We selected dye photosensitizers as antimicrobial additives for electrospinning,

79   because they produce highly reactive singlet oxygen ($^1O_2$) for effective and rapid virus disinfection,

80   they can be excited under the irradiation of visible light that is readily available in indoor

81   environments, they are low cost, and some of them have been approved by the U.S. Food and Drug

82   Administration for biomedical applications and thus pose little to no health risks to humans (e.g.,

83   rose bengal (RB)). Our membranes enable a self-cleaning feature for disinfecting coronaviruses

84   under ambient conditions, and photosensitized disinfection does not reduce the aerosol filtration

85   efficiency of the membranes. The photoreactive electrospun membranes can find broad air

86   filtration applications, such as face masks, respirators, and indoor air filters, and they are developed

87   for the first time for preventing the airborne transmission of SARS-CoV-2 and beyond.

88

89   We first optimized the composition for preparing the photosensitized electrospun nanofibrous

90   membranes to yield the best NaCl aerosol filtration efficiency, the lowest pressure drop in filtration,

91   and the highest reactivity for producing $^1O_2$ under visible light irradiation. Next, we tested the

92   filtration efficiency and inactivation kinetics of coronavirus aerosols to best understand

93   performance of the optimum membranes for controlling the airborne transmission of COVID-19.

94   We then conducted a thorough mechanistic investigation on how the membranes inactivated

95   coronaviruses, damaged viral genome, and impaired viral lifecycle in host cells. Last but not least,

96   to understand the lifetime of the membranes for practical engineering applications, we aged the

97   membranes under continuous light exposure up to 7 days and evaluated their long-term

98   performance of coronavirus aerosol filtration and coronavirus disinfection. Our promising results

99   highlighted that the photosensitized electrospun nanofibrous membranes showed outstanding

100   filtration performance for removing coronavirus aerosols, they rapidly disinfected coronaviruses

101   under visible light irradiation, and they maintained excellent performance when used in indoor

102   environments for a long duration.

103

2. Materials and Methods

104

2.1 Fabrication of photosensitized electrospun membranes

105

106   A series of two-layer photosensitized membranes were fabricated by electrospinning. Briefly, a

107   homogeneous electrospinning dope solution containing x wt% of polyvinylidene difluoride (PVDF)

108   ($x = 8$-20) and a dye photosensitizer in N,N-dimethylformamide/acetone (7/3, v/v) was electrospun

109   onto one layer of polypropylene (PP) fabrics (VWR® Basic Protection Face Mask). During the

110   electrospinning of 10-20 wt% of PVDF, the solution feeding rate, electric field, and

111   electrospinning duration was maintained at 0.6 mL h^{-1}, 1 kV cm^{-1}, and 20 min, respectively. For

112   electrospinning 8 wt% of PVDF, the solution feeding rate, electric field, and electrospinning

113   duration was kept at 0.4 mL h^{-1}, 1 kV cm^{-1}, and 30 min, respectively, to reduce bead formation.

114   The dyes including 0.3 wt% of RB, 0.015 wt% of methylene blue hydrate (MB), 0.3 wt% of crystal

115   violet (CV), 0.015 wt% of (-)-riboflavin (RF), and 0.003 wt% of toluidine blue O (TBO) were

116   used. Mass percentage of PVDF and the dyes was calculated with respect to the total mass of the

117   electrospinning dope solution, and the maximum dye concentration was selected based on dye

118   solubility in the solution. The two-layer photosensitized electrospun membranes were denoted as

119   PVDFx-dye name (e.g., PVDF15-RB). Membranes that were electrospun from 15 wt% of PVDF

120   without dyes onto a layer of PP fabrics (VWR® Basic Protection Face Mask) were also fabricated

121   for comparison (i.e., PVDF15).

122

123   Three-layer photosensitized electrospun membranes (here referred to as sandwiched membranes),

124   which consisted of an additional PP fabric top layer (Amazon, skin friendly non-woven fabrics)

125   on the top of the two-layer photosensitized electrospun membranes, were particularly assembled

126   for aerosol filtration and pressure drop tests. The sandwiched structure protected the electrospun

127   layer from destruction during and after filtration (e.g., removal from the filter holder). Based on

128   our previous study, the PP fabrics had negligible impact on aerosol removal and pressure drop,

129   because of their very large pore size compared with the aerosol size (~120 µm versus < 2 µm) and

130   high porosity.[12]

131

2.2 Characterization of photosensitized electrospun membranes

133   The nanofiber diameter of electrospun membranes was characterized by scanning electron

134   microscopy (SEM, FEI Teneo LV). For each membrane, at least 50 fibers were selected for

135   analyzing the diameter. The pore size of two-layer photosensitized electrospun membranes was

136   characterized by a gas liquid porometry method (POROLUXTM 100/200/500, shape factor of

137   0.715, APTCO Technologies LLC, Belgium). The pressure drop of sandwiched photosensitized

138   electrospun membranes was determined with a face velocity of 5.3 cm s^{-1}. Dye leaching from two-

139   layer photosensitized electrospun membranes was estimated by optical absorbance measurements

140   (UV-vis spectrophotometer, Hach DR6000), and details are in **Text S2**. $^1O_2$ production of the two-

141   layer photosensitized electrospun membranes was quantified in a liquid setup containing furfuryl

142   alcohol (FFA, 1 mM) under the exposure of both simulated reading light (100% 7W white LED

143   with a lamp-to-membrane distance of 15 cm) and simulated indoor light (3% 7W white LED with

144   a lamp-to-membrane distance of 33 cm), and the steady-state $^1O_2$ concentration ($[^1O_2]_{ss}$) was

145   calculated by dividing the measured first-order decay rate constant of FFA by the second-order

146   reaction rate constant between $^1O_2$ and FFA (1.2×10^8 M^{-1} s^{-1}). Simulated reading light had a

147   higher photon flux and optical power density than those of simulated indoor light, and they were

148   recorded in **Figure S1** and **Table S1** (AvaSpec-2048 Fiber Optic Spectrometer). FFA was

149   monitored by high performance liquid chromatography (Shimadzu LC-20AT Prominence).

150

151   **2.3 Determination of filtration efficiency for removing NaCl and coronavirus aerosols**

152   NaCl solution (0.1 M) and murine hepatitis virus A59 (MHV-A59) in water ($\sim 10^6$-10^7 gene copies

153   mL^{-1}, diluted from the virus stock by ~50 times with nuclease-free water) were used for

154   aerosolization and filtration tests. MHV-A59 was selected because it is a β-coronavirus that shares

155   the same family and the size with SARS-CoV-2 (85 nm of MHV-A59 versus 50-200 nm of SARS-

156   CoV-2).[14] Details of MHV-A59 propagation are in **Text S3**. Only for the aerosol size

157   characterization, aerosols were generated from ultrapure water containing polystyrene and silica

158   nanoparticles (00876-15, Polysciences; SISN100-25M, nanoComposix; both were 100 nm) to

159   simulate MHV-A59 aerosols, because both nanoparticles and the MHV-A59 had a similar size and

160   concentration during aerosolization and the two different nanoparticles had representative

161   hydrophobicity/hydrophilicity. In the filtration tests (i.e., filter-on), a portion of NaCl or MHV-

162   A59 aerosols were captured by the sandwiched membranes, whereas the penetrating aerosols were

163   retained by an impinger. In the control experiments (i.e., filter-off), no filter was in place and all

164   generated aerosols were retained by the impinger. The filtration efficiency was determined based

165   on the difference of the amount of NaCl or MHV-A59 in the impinger between filter-off and filter-

166   on experiments over the amount of NaCl or MHV-A59 in the impinger in the filter-off experiment.

167   At least duplicates were conducted for each filtration test and control experiment. Details of the

168   setup and experimental conditions are described in our previous study and also in **Text S4**.[12] NaCl

169 was quantified by ion chromatography (Dionex ICS-1100), and the amount and infectivity of

170 MHV-A59 were quantified by the reverse transcription-quantitative polymerase chain reaction

171 (RT-qPCR) and the integrated cell culture-reverse transcription-quantitative polymerase chain

172 reaction (ICC-RT-qPCR), respectively.

173

2.4 RT-qPCR quantification of coronaviruses

175 MHV-A59 collected in the impinger was concentrated by centrifugal ultrafiltration (Nanosep, 300

176 kDa, Pall Laboratory), and next proceeded for RNA extraction by a Zymo Quick-RNA Viral Kit

177 (R1035). MHV-A59 was quantified by RT-qPCR by amplifying a fraction of its ORF5 gene for

178 the structural protein M.[15,16] The TaqMan[TM] Fast Virus 1-Step Master Mix Kit (Thermo Fisher

179 Scientific Inc., 4444432) was used for RT-qPCR. Details of RNA extraction efficiency, the

180 sequence and concentration of primers, probe, and cDNA standard, reverse transcription and PCR

181 programs, PCR amplification efficiency, positive and negative controls, and inhibition tests are

182 summarized in **Text S5**. All the RT-qPCR data were reported following MIQE guidelines.[12,17]

183

2.5 Evaluation of coronavirus infectivity after photosensitization

185 Compared with conventional infectivity assays based on plaque forming units or median tissue

186 culture infectious dose (TCID$_{50}$), ICC-RT-qPCR is a rapid, sensitive, and reliable method for

187 quantifying the infectivity of coronaviruses, based on RT-qPCR of viral gene copy numbers after

188 virus replication in the host cells. The experimental conditions of ICC-RT-qPCR were optimized,

189 and the method is valid for quantifying the infectivity of MHV-A59 because a linear correlation

190 was observed between virus infectivity quantified by ICC-RT-qPCR and the viral load before

191 infection determined by RT-qPCR (**Figure S2**). Special attention should also be paid for

192 interpreting the virus infectivity quantified by ICC-RT-qPCR, because ICC-RT-qPCR compared

193 with a conventional cell culture assay could overestimate the dosage of reactive oxygen species

194 (ROS) to achieve the same level of virus inactivation.[18]

195

196 The infectivity of MHV-A59 captured on the photosensitized electrospun membrane was

197 evaluated by ICC-RT-qPCR after the exposure to simulated reading light. Briefly, the viruses on

198 the membrane were eluted in nuclease-free water, concentrated by centrifugal ultrafiltration

199 (Nanosep, 300 kDa, Pall Laboratory), and proceeded for cell infection and RT-qPCR

200 quantification. Details are included in **Text S6**. Unfortunately, the infectivity of MHV-A59 that

201 was eluted from the membrane after aerosol filtration was not able to be quantified by ICC-RT-

202 qPCR, because aerosolization lost most of the viruses (i.e., only ~1 out of a million viruses was

203 able to be aerosolized in our system) and a low multiplicity of infection did not allow virus

204 propagation in the host cells.[19] To facilitate quantifying the photoreactivity of photosensitized

205 electrospun membranes for inactivating MHV-A59, we designed a liquid setup that virus-laden

206 droplets were loaded on the membrane surface under the exposure of both simulated reading light

207 and simulated indoor light (details in **Text S7**). First-order infectivity decay rate constants, $k_{infectivity}$,

208 were obtained from the negative slope of the linear regression of the natural logarithm of MHV-

209 A59 infectivity versus the light exposure duration. The liquid setup was amended with a high viral

210 load, and it provided reliable and quantifiable infectivity of the virus after light exposure. The

211 liquid setup could best simulate the scenario of coronavirus inactivation when virus-laden

212 respiratory droplets are captured on the masks. Control experiments that evaluated MHV-A59

213 inactivation by PVDF15 under the irradiation of simulated reading light and by PVDF15-RB in

214   the dark were also conducted. Triplicates were conducted for MHV-A59 inactivation by PVDF15-

215   RB under light exposure, and duplicates were conducted for the control experiments.

216

2.6 Evaluation of coronavirus gene damage after photosensitization

218   After photosensitization, the ORF5 gene damage of both filter-captured MHV-A59 aerosols and

219   MHV-A59 in droplets was evaluated by RT-qPCR. The same experimental setup for investigating

220   MHV-A59 infectivity was used, as described in **Section 2.5**, and MHV-A59 aerosols captured on

221   the sandwiched PVDF15-RB and MHV-A59 droplets on PVDF15-RB were subjected to the

222   irradiation of simulated reading light. The samples were next collected at different time intervals

223   for RT-qPCR quantification, as described in **Section 2.4**. Photooxidation damaged the viral genes

224   and prevented its RT-qPCR quantification, and only the intact genes were able to be determined.

225   Control experiments that evaluated the ORF5 gene damage of captured MHV-A59 aerosols on

226   PVDF15 under the irradiation of simulated reading light and on PVDF15-RB in the dark were also

227   conducted. First-order ORF5 gene damage rate constants, k_{gene}, were obtained from the negative

228   slope of the linear regression of the natural logarithm of the ORF5 gene copy number quantified

229   by RT-qPCR versus the light exposure duration. Triplicates were conducted for the ORF5 gene

230   damage of MHV-A59 by PVDF15-RB under light exposure, including both viral aerosols and

231   droplets; and duplicates were conducted for the control experiments.

232

2.7 Evaluation of coronavirus' lifecycle after photosensitization

234   The impact of photosensitization on coronavirus' lifecycle in host cells, including virus binding

235   and internalization, was investigated. The same liquid setup as described in **Section 2.5** was used,

11

236 and MHV-A59 droplets on PVDF15-RB were subjected to the irradiation of simulated reading

237 light (details in **Text S8**). Incubation MHV-A59 with L-929 cells at 4 ℃ only allowed virus

238 binding, whereas subsequent increase of the incubation temperature to 37 ℃ permitted virus

239 internalization.[20–22] First-order rate constants of apparent damage to coronavirus' lifecycle were

240 obtained from negative slope of the linear regression of the natural logarithm of RT-qPCR

241 quantified viruses bound to and internalized into the cells versus the light exposure duration, and

242 they are denoted as $k_{app\_binding}$ and $k_{app\_internalization}$, respectively. The rate constants of true damage

243 to virus binding and internalization were calculated as $k_{binding}=k_{app\_binding}-k_{gene}$ and

244 $k_{internalization}=k_{app\_internalization}-k_{app\_binding}$, respectively.[18] The correction for $k_{app\_binding}$ was to

245 distinguish the decrease of ORF5 gene PCR signal due to ORF5 gene damage by photooxidation

246 and the loss of virus binding function by the same treatment; and the correction for $k_{app\_internalization}$

247 was to exclude the contribution of the decrease of ORF5 gene PCR signal due to damaged virus

248 binding by photosensitization. Triplicates were conducted for the damage of coronavirus' lifecycle

249 after photosensitization.

250

251 **2.8 Aging and robustness of photosensitized electrospun membranes**

252 Fresh two-layer photosensitized electrospun membranes were aged under different light exposure

253 to explore their robustness and lifetime for capturing and killing coronaviruses. Briefly, PVDF15-

254 RB was exposed to indoor light (fluorescent light in the laboratory) and simulated indoor light up

255 to 7 days and outdoor sunlight up to 4 days, and the aged membranes were denoted as PVDF-RB-

256 I, PVDF-RB-S, and PVDF-RB-O, respectively. The light spectrum and intensity for aging are

257 included in the **Figure S1** and **Table S1**. Particularly, indoor light and simulated indoor light had

258 almost identical photon flux and optical power density. After aging, the membranes were

259 characterized by SEM for morphology and nanofiber diameter, and their production of $^1O_2$ under

260 the irradiation of both simulated reading light and simulated indoor light was also measured, as

261 described in **Section 2.2**. Aged membranes were also used for testing the filtration efficiency for

262 removing MHV-A59 aerosols and the inactivation of MHV-A59 droplets, as described in **Sections**

263 **2.3** and **2.5**.

264

265 2.9 Data analysis

266 Student's t test was utilized to determine whether the calculated first-order reaction rate constants

267 of infectivity decay, ORF5 gene damage, and the damage of virus binding and internalization were

268 different from 0. Student's t test was also used for the statistical comparison of the difference

269 between two first-order reaction rate constants, $[^1O_2]_{ss}$, and aerosol filtration efficiencies. All p

270 values < 0.05 were considered statistically significant.

271

272 3. Results and Discussion

273 3.1 Optimizing photosensitized electrospun membranes

274 All photosensitized electrospun membranes showed the color of the photosensitizers, in contrast

275 to the white bare PVDF membranes, indicating the successful incorporation of photosensitizers

276 into the PVDF matrix (**Figure 1a**). The loading of photosensitizers was maximized based on their

277 solubility in the electrospinning dope solution to ensure the best photoreactivity for inactivating

278 coronaviruses. The hydrophilic photosensitizers were embedded in the hydrophobic PVDF, which

279 minimized photosensitizer leaching. Specifically, only 2.20 wt% of RB was released when

13

280 PVDF15-RB was immersed in water for 6 h, suggesting that the moisture from human breath or

281 ambient air would not induce significant photosensitizer leaching when the membranes are used

282 as masks and indoor air filters. To select the photosensitizer with the best photoreactivity, $[^1O_2]_{ss}$

283 produced from the electrospun membranes loaded with different photosensitizers was

284 characterized. Under the exposure of simulated reading light with a higher light intensity,

285 PVDF15-RB produced a $[^1O_2]_{ss}$ of $(6.94 \pm 2.19) \times 10^{-13}$ M, which was 2.31, 3.81, 8.68, and 4.08

286 times higher than that of PVDF15-MB, PVDF15-CV, PVDF15-RF, and PVDF15-TBO ($p < 0.05$,

287 **Figure S4**). Under the irradiation of simulated indoor light with a lower light intensity, PVDF15-

288 RB and PVDF15-MB outperformed other photosensitized electrospun membranes for producing

289 $^1O_2$ ($p < 0.05$, **Figure S4**). Therefore, RB was identified as the most photoreactive dye additive for

290 membrane fabrication. The fact that PVDF15-RB has the highest photoreactivity could be

291 attributed to the increased photon absorption under white LED light irradiation (maximum

292 absorption wavelength of RB is 546 nm) and a high quantum yield of the intersystem crossing of

293 RB for producing $^1O_2$.[23,24]

294

295 The PVDF concentration for developing photosensitized electrospun membranes was next

296 optimized to improve filtration performance. As the key factors determining the aerosol filtration

297 efficiency, the nanofiber diameter and pore size of the membranes were characterized at different

298 polymer concentrations. The nanofiber diameter of PVDF8-RB, PVDF10-RB, PVDF12-RB,

299 PVDF15-RB, PVDF18-RB, and PVDF20-RB was 60 ± 16, 116 ± 24, 164 ± 48, 196 ± 44, $521 \pm$

300 191, and 423 ± 114 nm, respectively (**Figure 1b**). Generally, the nanofiber diameter increased with

301 the increase of the PVDF concentration from 8 to 15 wt% and the membranes possessed uniform

302 nanofibers. When PVDF concentration reached to 18 and 20 wt% for electrospinning, the fibers

14

303   were not uniform anymore and some very large fibers were present. This could be attributed to a

304   significantly increased viscosity of the electrospinning dope solution and instable and non-

305   continuous electrospinning jets.[25] In addition, the nanofiber diameter and pore size of PVDF15-

306   RB (196 ± 44 nm, 1.46 ± 0.15 µm) was smaller than those of the bare electrospun membrane of

307   PVDF15 (315 ± 73 nm, 2.70 ± 0.20 µm), likely due to the presence of anionic RB and increased

308   conductivity of the dope solution for electrospinning.[12,26,27]

309

310   The filtration efficiency of NaCl aerosols was further examined for those PVDFx-RB membranes.

311   Our previous study has demonstrated the filtration efficiency of NaCl aerosols was a conservative

312   indicator for understanding the removal of coronavirus aerosols.[12] The average filtration efficiency

313   for NaCl aerosols was 98.2%, 99.2%, 98.8%, 99.1%, and 99.9% for PVDF8-RB, PVDF10-RB,

314   PVDF12-RB, PVDF15-RB, and PVDF18-RB, respectively (**Figure 1c**). PVDF20-RB was not

315   tested for filtering aerosols because the membrane was apparently non-uniform after

316   electrospinning. Pressure drop in filtration was also determined to understand the breathability or

317   energy consumption in filtration. With the increase of the PVDF concentration from 8 to 12 wt%

318   in the RB-sensitized electrospun membranes, the pressure drop increased from 0.47 ± 0.01 to 0.80

319   ± 0.05 inches of water column (inches wc). However, further increase of the PVDF concentration

320   from 12 to 18 wt% reduced the pressure drop to 0.16 ± 0.00 inches wc (**Figure 1c**). The low

321   pressure drop at a low PVDF concentration could be attributed to the slip effect of air molecules

322   on the ultrafine nanofibers, whereas the low pressure drop at a high PVDF concentration could be

323   resulted from a high membrane porosity.[28] PVDF15-RB had the best filtration performance

324   including a high aerosol filtration efficiency and a low pressure drop, the best photoreactivity in

325   terms of $^1O_2$ production, and uniform nanofibers across the whole membrane that allows

326   manufacturing at scale. Therefore, PVDF15-RB was selected for the following study of
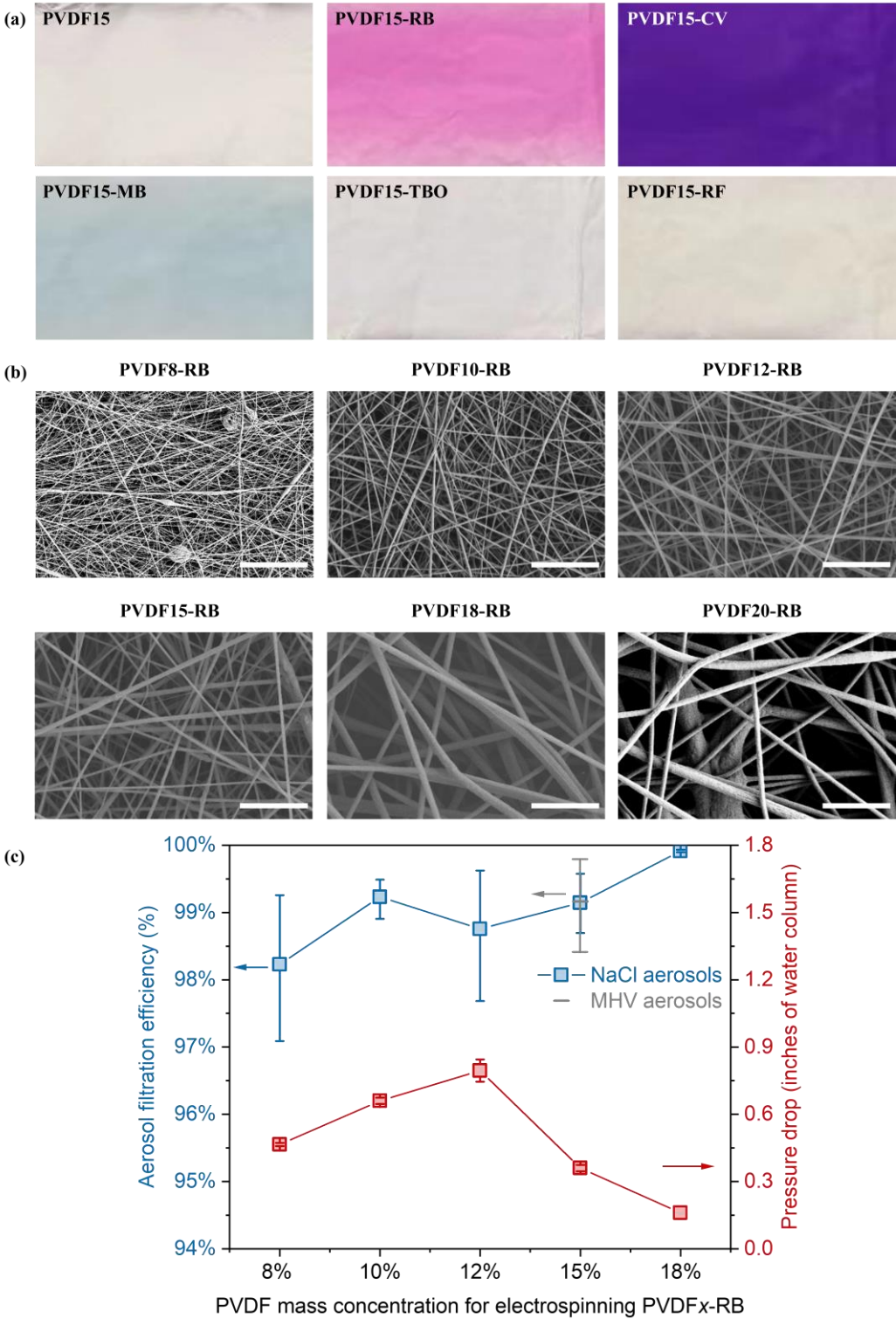
327   coronavirus filtration and inactivation.

(c)

328

329   **Figure 1.** (a) Photosensitized nanofibrous membranes electrospun with various photosensitizers;

330   (b) SEM for the RB-sensitized electrospun membranes with different PVDF concentrations. Scale

331   bars in SEM images are 5 µm; (c) NaCl and MHV-A59 aerosol filtration efficiency and pressure

332   drop in filtration for RB-sensitized electrospun membranes with different PVDF concentrations

333   (PVDF*x*-RB). Blue squares and error bars in the filtration efficiency graph represent average and

334   maximum/minimum values of duplicates, and red squares and error bars in the pressure drop graph

335   represent the average and standard deviation of triplicates.

336

337   **3.2 Photosensitized electrospun membranes for capturing and inactivating coronavirus**

338   **aerosols**

339   The optimized electrospun membrane of PVDF15-RB was further challenged by MHV-A59

340   aerosols, and it removed 99.2% of the viral aerosols on average (**Figure 1c**). The filtration

341   efficiency for MHV-A59 aerosols was on par with that for removing NaCl aerosols (99.1%, $p >$

342   0.05), and it was much higher compared with filtration efficiency of MHV-A59 aerosols by

343   commercial masks, including a surgical mask (98.2%), a cotton mask (73.3%), and a neck gaiter

344   (44.9 %).[12] The excellent aerosol filtration efficiency was resulted from the ultrafine nanofibers

345   and the small pore size of the electrospun membrane. Our previous study also reported that

346   PVDF15 captured 99.1% of the MHV-A59 aerosols,[12] which was comparable with that of

347   PVDF15-RB ($p > 0.05$). Size distribution of simulated MHV-A59 aerosols, generated from

348   polystyrene and silica nanoparticles in water, underscored that the most dominant aerosols were

349   in the size of 420-450 nm (**Figure S5**). Aerosol size characterization also highlighted that 79.9-

350   89.5% of the simulated MHV-A59 aerosols were between 200 and 500 nm (**Figure S5**) and they

351   were considered as the most penetrating aerosols in mechanical filtration.[29,30] The optimized

17

352   photosensitized electrospun membrane holds promise for effectively removing the most

353   challenging coronavirus aerosols, which could minimize and prevent the airborne transmission of

354   pathogens.

355

356   Beyond physical capture of the coronavirus aerosols, photosensitized electrospun membranes also

357   inactivated the captured coronaviruses under visible light irradiation through the rapid and potent

358   oxidation by $^1O_2$. The captured MHV-A59 aerosols on PVDF15-RB were exposed to the

359   irradiation of simulated reading light for 1 h, and the ORF5 gene copy number of MHV-A59 was

360   reduced by 93.7%, giving k_{gene} of 0.0461 ± 0.0044 min^{-1} (**Figures 2a** and **2b**). In contrast, in the

361   control experiments, no apparent ORF5 gene damage was observed when the photosensitizer or

362   the visible light was not present (**Figure S6**). These results indicated that the photosensitized

363   electrospun membranes damaged the coronavirus genome and could potentially inactivate the

364   viruses upon visible light exposure. However, only a small fraction of MHV-A59 genome was

365   quantified (~100 bases) in the RT-qPCR, and it could not represent or reveal the damage in other

366   regions in the whole genome (~31.5 kb). Different regions across the viral genome can contain

367   diverse nucleotide sequences and form unique secondary structures, which may have distinct

368   susceptibility to ROS oxidation.[31] A genome-wide approach that quantifies a large fraction of the

369   genome damage by PCR could be used to reasonably predict the whole genome damage upon

370   oxidation in the future.[32] More importantly, the quantity of the ORF5 gene determined by RT-

371   qPCR did not represent the viability of MHV-A59. During photosensitization, RB produces $^1O_2$

372   as the key ROS for inactivating viruses, through the oxidation of genomes, proteins, lipids, and

373   any other functional biomolecules of the viruses.[33,34] Because ROS are broad-spectrum oxidants

374   that damage multiple viral biomolecules at the same time and any critical damage could

375   compromise viral viability, virus infectivity was observed to decrease more quickly compared with

376   intact genes.[18] Therefore, the RT-qPCR quantification of intact genes can serve as a conservative

377   approach to understand virus infectivity, but the infectivity assay is needed to elucidate the

378   inactivation efficiency by the photosensitized electrospun membranes.

379

380   Though the ORF5 gene copy number of MHV-A59 aerosols was successfully quantified by RT-

381   qPCR with a high sensitivity, virus infectivity was below the detection limit of ICC-RT-qPCR

382   because only few coronaviruses were harvested from the membranes. The majority of

383   coronaviruses were lost during aerosolization, since the partitioning coefficient of the coronavirus

384   (the virus concentration in aerosols to that in the liquid solution for aerosolization) was only 5.80

385    $\pm 4.26 \times 10^{-7}$. To overcome the challenges in quantifying the viability of coronavirus aerosols, we

386   loaded MHV-A59 droplets (~ 1 mm thick) on PVDF15-RB and determined virus infectivity during

387   photosensitized disinfection. The setup best mimicked virus-laden respiratory droplets captured

388   by the masks, and it allowed the accurate quantification of virus infectivity because of a higher

389   concentration of MHV-A59 in the droplets than that in the aerosols. Under simulated reading light

390   exposure, we observed significant coronavirus inactivation, with $k_{infectivity}$ of 0.301 ± 0.052 min^{-1}

391   (**Figure 2** and **2b**). That is said, 98.9% of coronaviruses were inactivated after only 15 min

392   irradiation of the simulated reading light. In contrast, we did not see any noticeable coronavirus

393   inactivation under simulated indoor light exposure up to 30 min. Control experiments of PVDF15

394   under simulated reading light exposure and PVDF15-RB in the dark did not inactivate the

395   coronaviruses either (**Figure S7**). These results indicated that photosensitization with the presence

396   of both the dye and photons is needed for coronavirus inactivation. In addition, PVDF15-RB

397   produced more $^1O_2$ under the irradiation of simulated reading light than simulated indoor light

398   ([$^1O_2$]$_{ss}$ = (6.94 ± 2.19) × 10^{-13} versus (4.95 ± 0.80) × 10^{-14} M) (**Figure S4**), and thus much more

399   rapid coronavirus inactivation was observed under light exposure with a stronger intensity. We

400   also found that the ORF5 gene damage rate of MHV-A59 in the droplets was lower than that of

401   aerosolized MHV-A59 captured on the membranes after exposure to simulated reading light (k_{gene}

402   = 0.0195 ± 0.0030 versus 0.0461 ± 0.0044 min^{-1}, $p < 0.05$, **Figure 2** and **2b**). The slower ORF5

403   gene damage could be attributed to the shorter lifetime and diffusion length of $^1O_2$ in water

404   compared with that in the air (2 μs in distilled water versus 2.80 s in the air), due to energy

405   dissipation resulted from the collision between $^1O_2$ and water molecules.[35,36] The dissolved oxygen

406   concentration in water was also lower than the oxygen concentration in the air (< 10 mg L^{-1} in the

407   water versus 275 mg L^{-1} in the air at 25 °C), which might limit $^1O_2$ production in the aqueous

408   phase.[37] Since $^1O_2$ was the key ROS in photosensitization and it did not bias damaging the viral

409   genome and inactivating the viruses, the liquid setup is considered as a conservative system to

410   evaluate the inactivation of MHV-A59 aerosols captured on the photosensitized electrospun

411   membrane. Therefore, it is reasonable to speculate that the inactivation of infectious or viable

412   MHV-A59 in the aerosols captured on the membrane will be much faster than that in the droplets,

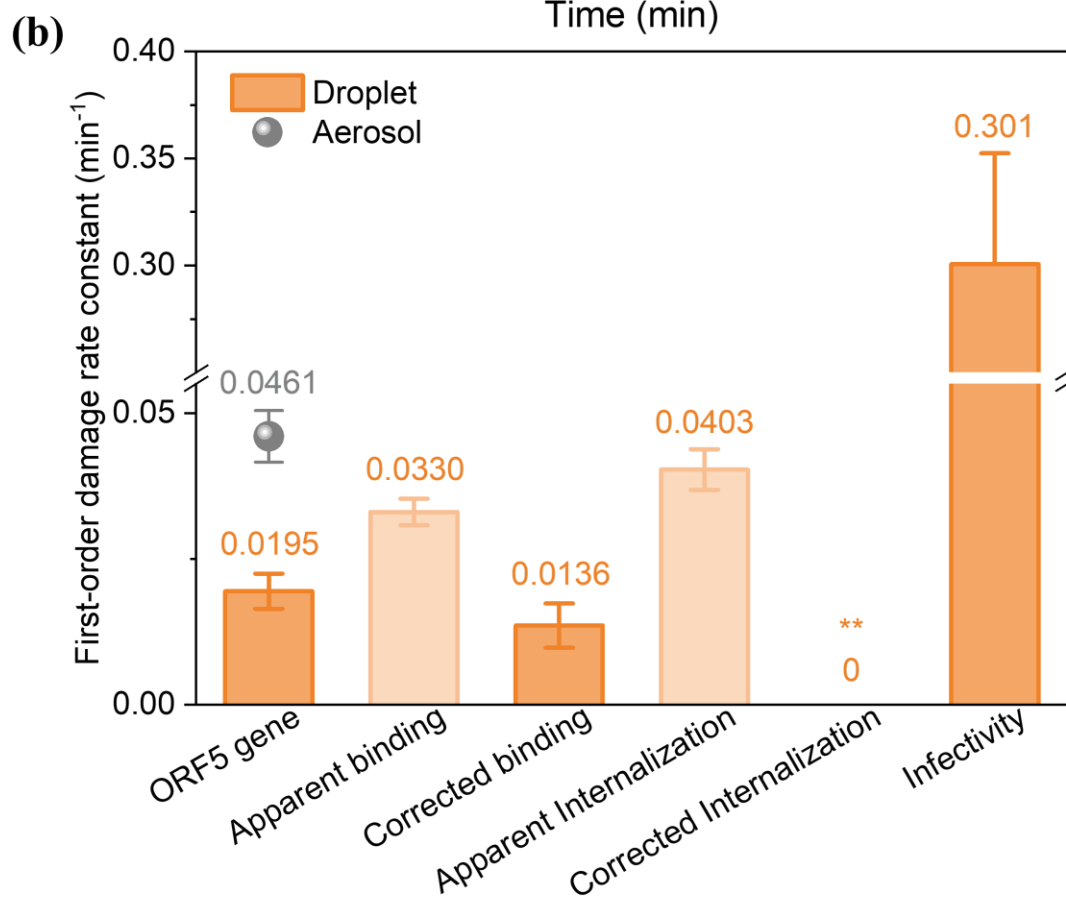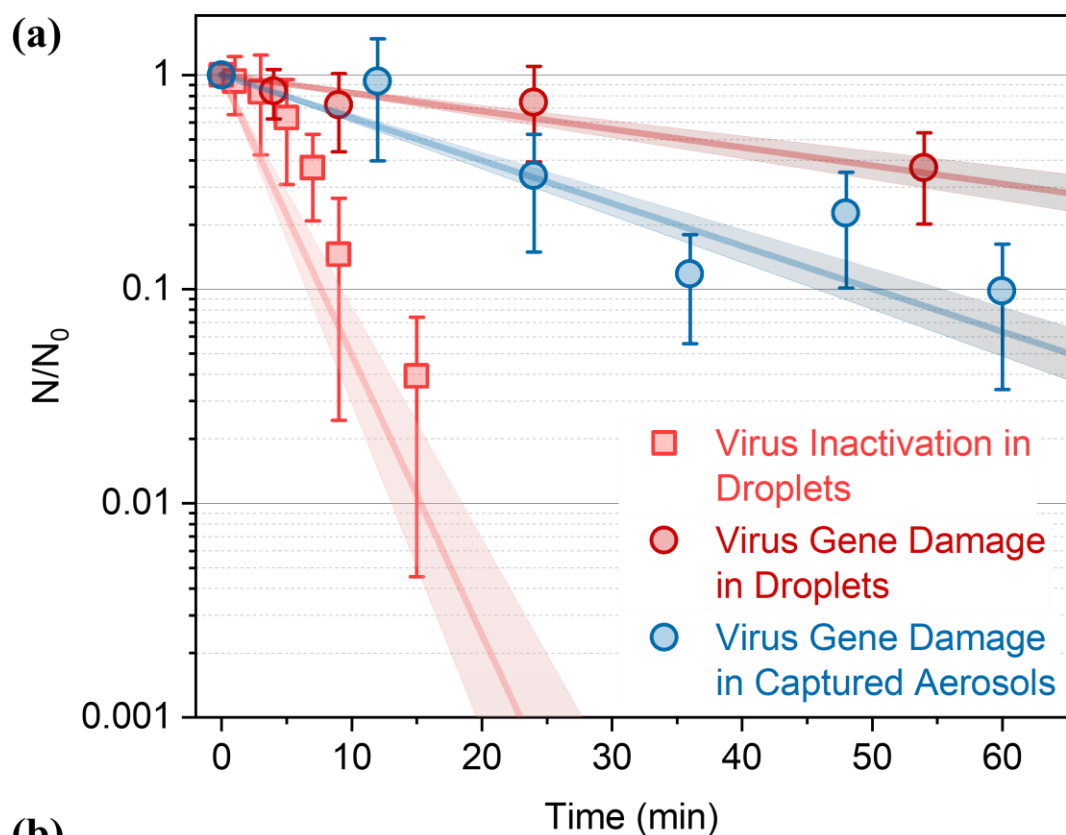413   though the infectivity of viral aerosols was not quantifiable in our study.

414

(a)

(b)

416   **Figure 2.** (a) First-order reaction kinetics of MHV-A59 infectivity decay in droplets and first-

417   order reaction kinetics of MHV-A59 ORF5 gene damage in both droplets and membrane-captured

418   aerosols. N/N_0 represents ORF5 gene copy numbers quantified by ICC-RT-qPCR (for infectivity)

419   or RT-qPCR (for gene damage) at light exposure duration t to that at light exposure duration zero.

420   Linear regression of common logarithm of N/N_0 versus light exposure duration and its standard

421   errors are illustrated. Error bars represent the standard deviation of triplicates. All tests were

422   conducted under simulated reading light exposure. (b) First-order damage rate constants for the

423   MHV-A59 ORF5 gene, and virus binding, internalization, and infectivity under simulated reading

424   light exposure. (**) denotes the rate constant was assigned a value of zero because there was no

425   statistical difference between the apparent damage rate constants of internalization and binding ($p >$

426   0.05). Error bars represent the standard error of the negative slope of linear regression.

427

3.3 Impact of photooxidation on the lifecycle of coronaviruses

429   We next investigated the effect of photosensitization on the lifecycle of coronaviruses in host cells,

430   particularly virus binding and internalization, to understand the impact of ROS on coronavirus

431   inactivation at a molecular level. For a viable MHV-A59, the viral spike (S) protein first binds to

432   the receptor of the host cells, murine carcinoembryonic antigen-related cell adhesion molecule 1a

433   (mCEACAM1a), and initiates the viral lifecycle.[38] Next, MHV-A59 transports RNA genomes into

434   the host cells by direct fusion of the viral envelope membrane with the cell plasma membrane, or

435   by endocytosis with subsequent fusion of the viral envelop membrane and the endosomal

436   membrane.[39] After internalization, viral genomes start replication as soon as sufficient machinery

437   proteins are produced. Once progeny viruses are constructed and assembled, they are released from

438   the old host cells and start their new lifecycle by infecting more host cells. It is clear that virus

22

439   binding and internalization are key steps that determine the fate and infectivity of coronaviruses,

440   and any damage to these biological processes could compromise the infectivity of the viruses.

441

442   We evaluated MHV-A59 binding and internalization in the liquid setup. Coronavirus binding to

443   the L-929 cells was impaired after photooxidation, and $k_{app\_binding}$ was estimated as 0.0330 ± 0.0023

444   min^{-1}. By excluding the contribution of ORF5 gene damage by oxidation ($k_{gene} = 0.0195 \pm 0.0030$

445   min^{-1}), the true decay rate constant of coronavirus binding ($k_{binding}$) was 0.0136 ± 0.0038 min^{-1} (p

446   < 0.05, **Figure 2b**). Coronavirus internalization into the L-929 cells is the subsequent step after

447   virus binding, therefore the difference between $k_{app\_internalization}$ and $k_{app\_binding}$ is considered as the

448   true damage to coronavirus internalization ($k_{internalization}$). However, photooxidation did not

449   compromise coronavirus internalization, because $k_{app\_internalization}$ and $k_{app\_binding}$ were statistically

450   the same (0.0403 ± 0.0035 versus 0.0330 ± 0.0023 min^{-1}, $p > 0.05$, **Figure 2b**). The S protein of

451   MHV-A59 plays important roles in both virus binding and internalization: the receptor-binding

452   domain in subunit 1 governs virus attachment to the host cells and the fusion peptide in subunit 2

453   is responsible for virus internalization.[38,40] $^1O_2$ produced in photosensitization non-selectively

454   oxidizes and damages viral biomolecules, including the S protein. However, we speculate that the

455   receptor-binding domain might be much more susceptible to $^1O_2$ oxidation compared with the

456   fusion peptide, because the latter contains a large amount of Ala and Gly that react with $^1O_2$

457   slowly.[41,42] It could explain why virus binding but not internalization was significantly impaired

458   after photosensitization, and further research is required.

459

460   **3.4 Aging of photosensitized electrospun membranes and their long-term performance**

23

461   Photosensitizers are generally sensitive to long-term light exposure, because the generated $^1O_2$ also

462   oxidizes the photosensitizers, leads to photobleaching, and reduces the photoreactivity for the

463   continuous production of $^1O_2$ and virus inactivation. After 4 days of sunlight exposure (including

464   both daytime and nighttime), the color of PVDF15-RB-O was significantly faded in comparison

465   to fresh PVDF15-RB. Nevertheless, after 7 days of continuous irradiation of simulated indoor light

466   and real indoor light, no apparent fading was observed for PVDF15-RB-S and PVDF15-RB-I

467   (**Figure 3a**). $^1O_2$ production was also characterized for all these aged membranes, and $[^1O_2]_{ss}$ was

468   $(2.26 \pm 0.11) \times 10^{-13}$, $(5.64 \pm 1.18) \times 10^{-13}$, and $(7.75 \pm 1.70) \times 10^{-13}$ M for PVDF15-RB-O,

469   PVDF15-RB-S, PVDF15-RB-I, respectively, under the scenario of simulated reading light

470   exposure (**Figure S4**). Significant less $^1O_2$ production was observed for PVDF15-RB-O when

471   compared to PVDF15-RB ($p < 0.05$), but a similar amount of $^1O_2$ was generated from PVDF15-

472   RB, PVDF15-RB-S, and PVDF15-RB-I (all $p > 0.05$). Membrane morphology was also

473   characterized, but aging under light exposure for extended duration did not change the nanofiber

474   diameter: the diameters were 203 ± 51, 200 ± 43, and 183 ± 45 nm for PVDF15-RB-I, PVDF15-

475   RB-S, and PVDF15-RB-O, respectively, in comparison with the fresh PVDF15-RB with a fiber

476   diameter of 196 ± 44 nm (**Figure 3a**).

477

478   Aged membranes were subjected for MHV-A59 aerosol filtration tests, and they all showed high

479   filtration performance: the average filtration efficiency of PVDF15-RB-I, PVDF15-RB-S, and

480   PVDF15-RB-O was 99.97, 99.96, and 99.95%, respectively. Aging under extended light exposure

481   did not physically damage the membranes, and thus the aged membranes maintained excellent

482   performance for removing MHV-A59 aerosols. However, aging did compromise membrane

483   performance for coronavirus inactivation, particularly the significantly faded membrane after

484   sunlight aging: PVDF15-RB-O inactivated MHV-A59 in droplets with $k_{infectivity}$ only of $0.0273 \pm$

485   0.0079 min^{-1}, which was 11.0 times lower than that of PVDF15-RB (0.301 ± 0.052 min^{-1}, both

486   tested under simulated reading light irradiation, $p < 0.05$, **Figure 3b**). In contrast, PVDF15-RB-S

487   that did not fade after the aging by simulated indoor light kept its photoreactivity, and it inactivated

488   MHV-A59 in droplets with $k_{infectivity}$ of 0.268 ± 0.0386 min^{-1}, which was comparable with that of

489   PVDF15-RB (also tested under simulated reading light irradiation, $p > 0.05$). Fast coronavirus

490   inactivation kinetics could be attributed to a higher $[^1O_2]_{ss}$ produced by the membranes (**Figure**

491   **3b**). Since humans spend most of their time indoor and the risk of COVID-19 airborne

492   transmission is much higher for indoor than outdoor activities, our results underscored that when

493   used for face masks the photosensitized electrospun membranes could maintain their excellent

494   performance of coronavirus aerosol filtration and coronavirus inactivation for a long duration
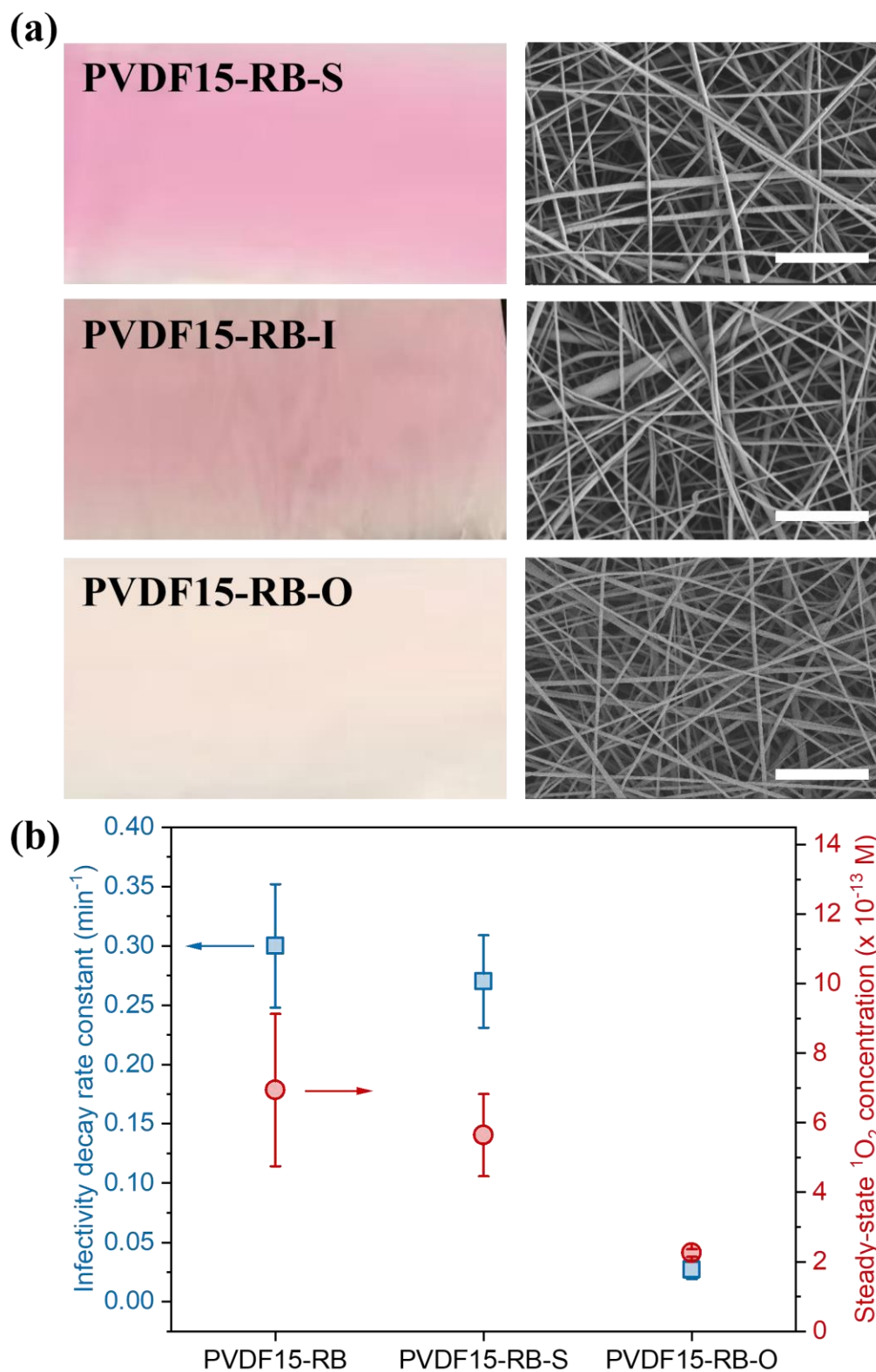
495   under indoor light exposure.

496

497 **Figure 3.** (a) Photos and SEM images of PVDF15-RB membranes after aging. Scale bars in the

498 SEM images are 5 µm; (b) first-order decay rate constants of MHV-A59 infectivity in droplets and

499 the corresponding $^1O_2$ production on fresh and aged PVDF15-RB membranes. All tests of virus

500 inactivation and $^1O_2$ production were conducted under the irradiation of simulated reading light.

501 Error bars for the infectivity decay rate constant represent the standard error of the negative slope

502 of the linear regression of common logarithm of infectivity versus light exposure duration, and

503 error bars for the steady-state $^1O_2$ concentration represent the standard deviation of triplicate

504 measurements.

505

4. Environmental Implication

507 Our study leverages nanotechnology to advance the design and fabrication of masks, respirators,

508 and air filters, and it addresses the grand challenge of the airborne transmission of COVID-19.

509 Photosensitized electrospun membranes showed excellent performance for capturing and killing

510 coronavirus aerosols, i.e., they removed 99.2% of MHV-A59 aerosols, and inactivated 98.9% of

511 MHV-A59 droplets only after 15 min of desk lamp irradiation. Electrospinning is an industrial

512 viable and economically feasible technology for manufacturing new air filtration media at scale

513 that could outperform current products on the market,[43,44] such as cloth face masks and indoor air

514 filters, for filtering out airborne pathogens. Miniaturized and portable electrospinning apparatuses

515 further facilitate the wide deployment of the technique for individuals and small communities.[45]

516 Moreover, integration of dye photosensitizers as effective, low-cost, and biocompatible

517 antimicrobial additives enables easy decontamination of air filtration media in and after use.

518 Compared with many other disinfection strategies for reusing the masks and respirators in the

519 COVID-19 pandemic, such as the treatment by heat, ultraviolet light irradiation, ozone, or

27

520   hydrogen peroxide vapor,[46–48] photosensitized electrospun air filters generate broad-spectrum

521   biocides of $^1O_2$ *in situ* under visible light exposure at the room temperature and pressure, and $^1O_2$

522   could potentially damage multiple viral biomolecules and multiple steps in viral lifecycle to

523   effectively inactivate coronaviruses. Photosensitized disinfection is less chemical and energy

524   intensive, and it does not compromise the aerosol filtration efficiency after disinfection. In addition,

525   color intensity and fading of the dye photosensitizers could serve as an indicator of the

526   antimicrobial lifetime of the air filtration media.[49]

527

528   Future studies should focus on developing robust photoreactive air filters with extended lifetime

529   to overcome the challenges of photobleaching of the dye-sensitized membranes, e.g., replacing the

530   dyes with stable visible-light-responsive photocatalysts. In addition, further elucidating the

531   mechanism of ROS damage to the coronaviruses will provide fundamental insights on designing

532   advanced antimicrobial air filters.

533

534   **Acknowledgements**

540

ASSOCIATED CONTENT

Supporting Information

Experimental details; spectral irradiance, photon flux, and optical power density of the light sources; linear correlation of MHV-A59 infectivity with the viral load before infection; steady-state $^1O_2$ concentrations produced by photosensitized electrospun air filters; aerosol size distribution; ORF5 gene damage of MHV-A59 aerosols in control experiments; infectivity of MHV-A59 droplets in control experiments.

Reference

(1)   CDC. Coronavirus disease 2019 (COVID-19). https://www.cdc.gov/coronavirus/2019-ncov/science/science-briefs/sars-cov-2-transmission.html.

(2)   Transmission of SARS-CoV-2: implications for infection prevention precautions: scientific brief, 09 July 2020. https://apps.who.int/iris/handle/10665/333114.

(3)   van Doremalen, N.; Bushmaker, T.; Morris, D. H.; Holbrook, M. G.; Gamble, A.; Williamson, B. N.; Tamin, A.; Harcourt, J. L.; Thornburg, N. J.; Gerber, S. I.; Lloyd-Smith, J. O.; de Wit, E.; Munster, V. J. Aerosol and surface stability of SARS-CoV-2 as compared with SARS-CoV-1. *N. Engl. J. Med.* **2020**, *382* (16), 1564–1567.

(4)   Rowan, N. J.; Moral, R. A. Disposable face masks and reusable face coverings as non-pharmaceutical interventions (NPIs) to prevent transmission of SARS-CoV-2 variants that cause coronavirus disease (COVID-19): role of new sustainable NPI design innovations and predictive mathematical modelling. *Sci. Total Environ.* **2021**, *772*, 145530.

(5)   Kwon, S.; Joshi, A. D.; Lo, C.-H.; Drew, D. A.; Nguyen, L. H.; Guo, C.-G.; Ma, W.; Mehta, R. S.; Shebl, F. M.; Warner, E. T.; Astley, C. M.; Merino, J.; Murray, B.; Wolf, J.; Ourselin, S.; Steves, C. J.; Spector, T. D.; Hart, J. E.; Song, M.; VoPham, T.; Chan, A. T. Association of social distancing and face mask use with risk of COVID-19. *Nat. Commun.* **2021**, *12* (1), 3737.

(6)   Cheng, Y.; Ma, N.; Witt, C.; Rapp, S.; Wild, P. S.; Andreae, M. O.; Pöschl, U.; Su, H. Face masks effectively limit the probability of SARS-CoV-2 transmission. *Science* **2021**, *372* (6549), 1439–1443.

(7)   Matulevicius, J.; Kliucininkas, L.; Prasauskas, T.; Buivydiene, D.; Martuzevicius, D. The comparative study of aerosol filtration by electrospun polyamide, polyvinyl acetate, polyacrylonitrile and cellulose acetate nanofiber media. *J. Aerosol Sci.* **2016**, *92*, 27–37.

(8)   Choi, J.; Yang, B. J.; Bae, G.-N.; Jung, J. H. Herbal extract incorporated nanofiber fabricated by an electrospinning technique and its application to antimicrobial air filtration. *ACS Appl. Mater. Interfaces* **2015**, *7* (45), 25313–25320.

(9)   Leung, W. W. F.; Sun, Q. Electrostatic charged nanofiber filter for filtering airborne novel coronavirus (COVID-19) and nano-aerosols. *Sep. Purif. Technol.* **2020**, *250*, 116886.

(10)   Lovera, D.; Bilbao, C.; Schreier, P.; Kador, L.; Schmidt, H.-W.; Altstädt, V. Charge storage of electrospun fiber mats of poly(phenylene ether)/polystyrene blends. *Polym. Eng. Sci.* **2009**, *49* (12), 2430–2439.

(11)   Gao, H.; He, W.; Zhao, Y.-B.; Opris, D. M.; Xu, G.; Wang, J. Electret mechanisms and kinetics of electrospun nanofiber membranes and lifetime in filtration applications in comparison with corona-charged membranes. *J. Membr. Sci.* **2020**, *600*, 117879.

(12)   Shen, H.; Zhou, Z.; Wang, H.; Zhang, M.; Han, M.; Durkin, D. P.; Shuai, D.; Shen, Y. Development of electrospun nanofibrous filters for controlling coronavirus aerosols. *Environ. Sci. Technol. Lett.* **2021**. https://doi.org/10.1021/acs.estlett.1c00337.

(13)   Blachere, F. M.; Lindsley, W. G.; McMillen, C. M.; Beezhold, D. H.; Fisher, E. M.; Shaffer, R. E.; Noti, J. D. Assessment of influenza virus exposure and recovery from contaminated surgical masks and N95 respirators. *J. Virol. Methods* **2018**, *260*, 98–106.

(14)   Bárcena, M.; Oostergetel, G. T.; Bartelink, W.; Faas, F. G. A.; Verkleij, A.; Rottier, P. J. M.; Koster, A. J.; Bosch, B. J. Cryo-electron tomography of mouse hepatitis virus: insights into the structure of the coronavirion. *Proc. Natl. Acad. Sci. U.S.A.* **2009**, *106* (2), 582–587.

(15)   Besselsen, D. G.; Wagner, A. M.; Loganbill, J. K. Detection of rodent coronaviruses by use of fluorogenic reverse transcriptase-polymerase chain reaction analysis. *Comp. Med.* **2002**, *52* (2), 111–116.

(16)   Yoo, D.; Pei, Y.; Christie, N.; Cooper, M. Primary structure of the sialodacryoadenitis virus genome: sequence of the structural-protein region and its application for differential diagnosis. *Clin. Diagn. Lab. Immunol.* **2000**, *7* (4), 568–573.

(17)   Bustin, S. A.; Benes, V.; Garson, J. A.; Hellemans, J.; Huggett, J.; Kubista, M.; Mueller, R.; Nolan, T.; Pfaffl, M. W.; Shipley, G. L.; Vandesompele, J.; Wittwer, C. T. The MIQE guidelines: minimum information for publication of quantitative real-time PCR experiments. *Clin. Chem.* **2009**, *55* (4), 611–622.

(18)   Romero-Maraccini, O. C.; Shisler, J. L.; Nguyen, T. H. Solar and temperature treatments affect the ability of human rotavirus Wa to bind to host cells and synthesize viral RNA. *Appl. Environ. Microbiol.* **2015**, *81* (12), 4090–4097.

(19)   Altan-Bonnet, N.; Perales, C.; Domingo, E. Extracellular vesicles: vehicles of *en bloc* viral transmission. *Virus Res.* **2019**, *265*, 143–149.

(20)   Bönsch, C.; Zuercher, C.; Lieby, P.; Kempf, C.; Ros, C. The Globoside receptor triggers structural changes in the B19 virus capsid that facilitate virus internalization. *J. Virol.* **2020**, 84 (22), 11737-11746.

(21)   Hackett, B. A.; Cherry, S. Flavivirus internalization is regulated by a size-dependent endocytic pathway. *Proc. Natl. Acad. Sci. U.S.A.* **2018**, *115* (16), 4246–4251.

(22)   Hackett, B. A.; Yasunaga, A.; Panda, D.; Tartell, M. A.; Hopkins, K. C.; Hensley, S. E.; Cherry, S. RNASEK is required for internalization of diverse acid-dependent viruses. *Proc. Natl. Acad. Sci. U.S.A.* **2015**, *112* (25), 7797–7802.

(23)   Murasecco-Suardi, P.; Gassmann, E.; Braun, A. M.; Oliveros, E. Determination of the quantum yield of intersystem crossing of rose bengal. *Helvetica Chimica Acta.* **1987**, *70* (7), 1760–1773.

(24)   Rauf, M. A.; Graham, J. P.; Bukallah, S. B.; Al-Saedi, M. A. S. Solvatochromic behavior on the absorption and fluorescence spectra of rose bengal dye in various solvents. *Spectrochim. Acta A Mol. Biomol. Spectrosc.* **2009**, *72* (1), 133–137.

(25)   Gupta, P.; Elkins, C.; Long, T. E.; Wilkes, G. L. Electrospinning of linear homopolymers of poly(methyl methacrylate): exploring relationships between fiber formation, viscosity, molecular weight and concentration in a good solvent. *Polymer* **2005**, *46* (13), 4799–4810.

(26)   Angammana, C. J.; Jayaram, S. H. Analysis of the effects of solution conductivity on electrospinning process and fiber morphology. *IEEE Trans. Ind. Appl.* **2011**, *47* (3), 1109–1117.

(27)   Choi, J. S.; Lee, S. W.; Jeong, L.; Bae, S.-H.; Min, B. C.; Youk, J. H.; Park, W. H. Effect of organosoluble salts on the nanofibrous structure of electrospun poly(3-hydroxybutyrate-*co*-3-hydroxyvalerate). *Int. J. Biol. Macromol.* **2004**, *34* (4), 249–256.

(28)   Zhao, X.; Wang, S.; Yin, X.; Yu, J.; Ding, B. Slip-effect functional air filter for efficient purification of $PM_{2.5}$. *Sci Rep.* **2016**, *6* (1), 35472.

(29)   Podgórski, A.; Bałazy, A.; Gradoń, L. Application of nanofibers to improve the filtration efficiency of the most penetrating aerosol particles in fibrous filters. *Chem. Eng. Sci.* **2006**, *61* (20), 6804–6815.

(30)   He, X.; Reponen, T.; McKay, R. T.; Grinshpun, S. A. Effect of particle size on the performance of an N95 filtering facepiece respirator and a surgical mask at various breathing conditions. *Aerosol Sci. Technol.* **2013**, *47* (11), 1180–1187.

(31)   Chang, R. L.; Stanley, J. A.; Robinson, M. C.; Sher, J. W.; Li, Z.; Chan, Y. A.; Omdahl, A. R.; Wattiez, R.; Godzik, A.; Matallana-Surget, S. Protein structure, amino acid composition and sequence determine proteome vulnerability to oxidation-induced damage. *EMBO J.* **2020**, *39* (23), e104523.

(32)   Rockey, N.; Young, S.; Kohn, T.; Pecson, B.; Wobus, C. E.; Raskin, L.; Wigginton, K. R. UV disinfection of human norovirus: evaluating infectivity using a genome-wide PCR-based approach. *Environ. Sci. Technol.* **2020**, 54 (5), 2851-2858.

(33)   Kim, J.; Lee, H.; Lee, J.-Y.; Park, K.-H.; Kim, W.; Lee, J. H.; Kang, H.-J.; Hong, S. W.; Park, H.-J.; Lee, S.; Lee, J.-H.; Park, H.-D.; Kim, J. Y.; Jeong, Y. W.; Lee, J. Photosensitized production of singlet oxygen via C_{60} fullerene covalently attached to functionalized silica-coated stainless-steel mesh: remote bacterial and viral inactivation. *Appl. Catal. B* **2020**, *270*, 118862.

(34)   Li, Y.; Zhang, C.; Shuai, D.; Naraginti, S.; Wang, D.; Zhang, W. Visible-light-driven photocatalytic inactivation of MS2 by metal-free g-C_3N_4: virucidal performance and mechanism. *Water Res.* **2016**, *106*, 249–258.

(35)   Wang, K.-K.; Song, S.; Jung, S.-J.; Hwang, J.-W.; Kim, M.-G.; Kim, J.-H.; Sung, J.; Lee, J.-K.; Kim, Y.-R. Lifetime and diffusion distance of singlet oxygen in air under everyday atmospheric conditions. *Phys. Chem. Chem. Phys.* **2020**, *22* (38), 21664–21671.

(36)   Merkel, P. B.; Kearns, D. R. Radiationless decay of singlet molecular oxygen in solution. Experimental and theoretical study of electronic-to-vibrational energy transfer. *J. Am. Chem. Soc.* **1972**, *94* (21), 7244–7253.

(37)   Wang, L. K.; Vielkind, D.; Wang, M. H. Mathematical models of dissolved oxygen concentration in fresh water. *Ecol. Modell.* **1978**, *5* (2), 115–123.

(38)   Peng, G.; Sun, D.; Rajashankar, K. R.; Qian, Z.; Holmes, K. V.; Li, F. Crystal structure of mouse coronavirus receptor-binding domain complexed with its murine receptor. *Proc. Natl. Acad. Sci. U.S.A.* **2011**, *108* (26), 10696–10701.

(39)   Burrell, C. J.; Howard, C. R.; Murphy, F. A. Coronaviruses. *Fenner and White's Medical Virology* **2017**, 437–446.

(40)   Luo, Z.; Weiss, S. R. Roles in cell-to-cell fusion of two conserved hydrophobic regions in the murine coronavirus spike protein. *Virol.* **1998**, *244* (2), 483–494.

(41)   J. Davies, M. Reactive species formed on proteins exposed to singlet oxygen. *Photochem. Photobiol. Sci.* **2004**, *3* (1), 17–25.

(42)   Sjöberg, B.; Foley, S.; Staicu, A.; Pascu, A.; Pascu, M.; Enescu, M. Protein reactivity with singlet oxygen: influence of the solvent exposure of the reactive amino acid residues. *J. Photochem. Photobiol. B* **2016**, *159*, 106–110.

(43)   Yu, M.; Dong, R.; Yan, X.; Yu, G.; You, M.; Ning, X.; Long, Y. Recent advances in needleless electrospinning of ultrathin fibers: from academia to industrial production. *Macromol. Mater. Eng.* **2017**, 302 (7), 1700002.

(44)   Persano, L.; Camposeo, A.; Tekmen, C.; Pisignano, D. Industrial upscaling of electrospinning and applications of polymer nanofibers: a review. *Macromol. Mater. Eng.* **2013**, 298 (5), 504-520.

677   (45)   Mouthuy, P.-A.; Groszkowski, L.; Ye, H. Performances of a portable electrospinning
678   apparatus. *Biotechnol. Lett.* **2015**, *37* (5), 1107–1116.

679   (46)   Dennis, R.; Pourdeyhimi, B.; Cashion, A.; Emanuel, S.; Hubbard, D. Durability of
680   disposable N95 mask material when exposed to improvised ozone gas disinfection. *JoSaM.* **2020**,
681   *2* (1).

682   (47)   Rubio-Romero, J. C.; Pardo-Ferreira, M. del C.; Torrecilla-García, J. A.; Calero-Castro, S.
683   Disposable masks: disinfection and sterilization for reuse, and non-certified manufacturing, in the
684   face of shortages during the COVID-19 pandemic. *Saf. Sci.* **2020**, *129*, 104830.

685   (48)   Oh, C.; Araud, E.; Puthussery, J. V.; Bai, H.; Clark, G. G.; Wang, L.; Verma, V.; Nguyen,
686   T. H. Dry heat as a decontamination method for N95 respirator reuse. *Environ. Sci. Technol. Lett.*
687   **2020**, *7* (9), 677–682.

688   (49)   Ryberg, E. C.; Chu, C.; Kim, J.-H. Edible dye-enhanced solar disinfection with safety
689   indication. *Environ. Sci. Technol.* **2018**, *52* (22), 13361–13369.

690

691

692

693

694

695

696

697